Finite element computation of elliptical vocal tract impedances using the two-microphone transfer function method

Marc Arnela and Oriol Guasch[a)]
GTM Grup de recerca en Tecnologies Mèdia, La Salle, Universitat Ramon Llull, C/Quatre Camins 2, Barcelona 08022, Catalonia, Spain.

(Received 15 November 2012; revised 26 March 2013; accepted 15 April 2013)

A two-microphone transfer function (TMTF) method is adapted to a numerical framework to compute the radiation and input impedances of three-dimensional vocal tracts of elliptical cross-section. In its simplest version, the TMTF method only requires measuring the acoustic pressure at two points in an impedance duct and the postprocessing of the corresponding transfer function. However, some considerations are to be taken into account when using the TMTF method in the numerical context, which constitute the main objective of this paper. In particular, the importance of including absorption at the impedance duct walls to avoid lengthy numerical simulations is discussed and analytical complex axial wave numbers for elliptical ducts are derived for this purpose. It is also shown how the direct impedance of plane wave propagation can be computed beyond the TMTF maximum threshold frequency by appropriate location of the virtual microphones. Virtual microphone spacing is also discussed on the basis of the so-called singularity factor. Numerical examples include the computation of the radiation impedance of vowels /a/, /i/, and /u/ and the input impedance of vowel /a/, for simplified vocal tracts of circular and elliptical cross-sections. © *2013 Acoustical Society of America*.
[http://dx.doi.org/10.1121/1.4803889]

PACS number(s): 43.70.Bk, 43.20.Mv [BHS] Pages: 4197–4209

I. INTRODUCTION

Radiation and input impedances of vocal tracts are of special interest for voice production. They play a significant role in determining wave radiation at the lip termination or in modeling the acoustic coupling of the vocal tract and the vocal folds. Impedances can be computed from numerical simulations of vocal tract acoustics. Because of intricate geometry of the vocal tract the finite element method (FEM) is an appropriate numerical approach to carry out these simulations. Several works can be found in literature dealing with FEM computations both in the frequency domain (e.g., Matsuzaki *et al.*, 2000; Motoki, 2002; Hannukainen *et al.*, 2007) and time domain (e.g., Švancara and Horáček, 2006; Vampola *et al.*, 2008, 2011). Occasionally other approaches such as finite differences have also been used (e.g., Takemoto *et al.*, 2010).

With regards to voice production, working in the time domain turns to be a very appealing option given that time evolving phenomena such as the self-oscillation of the vocal folds, the generation of diphthongs, or the visualization of acoustic waves propagating through the vocal tract and generation of corresponding audio files, could be naturally accounted for in numerical simulations. If the wave equation is solved in its mixed form (e.g., Takemoto *et al.*, 2010; Codina, 2008), impedances can be directly computed from the Fourier transforms of the acoustic pressure and acoustic velocity time evolutions. However, this is not possible if the wave equation is solved in irreducible form for the acoustic pressure (e.g., Vampola *et al.*, 2011) or for the velocity potential (e.g., Matsuzaki *et al.*, 2000). In such cases the acoustic velocity has to be computed from the acoustic pressure or the velocity potential gradients. This is not difficult for structured meshes, but it is not so straightforward for unstructured meshes, elemental integration, and assembly being required in addition at each time step for the pressure/velocity ratio at the radiation surface, in order to obtain the impedance.

In this paper an alternative is proposed for a straightforward computation of the plane wave radiation and input impedances of vocal tracts, that requires no knowledge of the acoustic velocity field. The idea is to adapt the experimental two-microphone transfer function (TMTF) method to the numerical framework. Originally developed by Chung and Blaser (1980), the simplest version of the TMTF method only requires measuring the time evolution of the acoustic pressure at two points in an impedance duct, and computing the corresponding transfer function. From this transfer function, the radiation and/or input impedances at a given surface can be easily derived. In return, the price to be paid for such a simple approach is that an additional simulation substituting the vocal tract with an impedance duct has to be performed for the computation of radiation impedances (this is not the case for input impedances where an impedance duct is always coupled at the entry of the vocal tract, whatever numerical approach is followed). The purpose of this study was to develop the TMTF method for computing vocal tract impedances in a numerical environment. First, it will be shown that dealing with lossy impedance ducts reduces the overall time duration of the simulations. The inclusion of wall losses allows for strong attenuation of the first duct eigenmode, which otherwise determines the total duration of the computation. However, this implies using appropriate

[a)]Author to whom correspondence should be addressed. Electronic mail: oguasch@salle.url.edu

complex wave numbers in the TMTF expressions, which are well-known for three-dimensional circular cylindrical ducts, and which will be derived in this work for elliptical cross sectional impedance ducts, given their importance in voice production (see, e.g., Motoki, 2002; Matsuzaki *et al.*, 2000, where elliptical vocal tracts are used). Second, the frequency range of validity of the TMTF method will be analyzed. Specifically, it will be shown how the direct impedance of plane wave propagation can be computed beyond the TMTF maximum threshold frequency by appropriate location of the virtual microphones (mesh nodes where the acoustic pressure time evolution is collected). In addition, the appropriate virtual microphone spacing will be determined by means of the so called singularity factor (SF) introduced by Jang and Ih (1998), according to the maximum frequency of analysis. Throughout the work, time domain FEM simulations for the irreducible wave equation will be performed with custom software, to compute vocal tract impedances using the adapted TMTF method. However, any other time domain numerical approach could benefit from the reported results. A preliminary version was presented in Arnela and Guasch (2012).

The paper is organized as follows. Section II presents the methodology for computing the acoustic impedance of vocal tracts from numerical simulations. In Sec. III, the various considerations to be taken into account when adapting the TMTF method to the numerical framework are analyzed. Numerical examples of computed impedances for vocal tracts of circular and elliptical cross-section are provided in Sec. IV. Finally, conclusions close the paper in Sec. V.

II. METHODOLOGY

A. The two-microphone transfer function method

The TMTF was originally developed by Chung and Blaser (1980) and later on standardized in the ISO 10534-2 (1998) for measuring the normal reflection coefficient of material samples. The normalized specific acoustic impedance Z can be obtained from the latter. The TMTF proceeds as follows. First, plane waves are generated at the entrance of a duct of length L, referred to as the impedance duct. The acoustic pressure signals $P_1(f)$ and $P_2(f)$ are measured at two points x_1 and x_2 close to the impedance duct exit, which is designated as the reference surface, and the transfer function $H_{12}(f) = P_2(f)/P_1(f)$ is computed. The reflection coefficient $\mathcal{R}_1$ at position x_1 is given by

$$\mathcal{R}_1 = \frac{H_{12} - H_I}{H_R - H_{12}}, \tag{1}$$

with H_I and H_R, respectively, standing for the incident and reflected wave transfer functions. Assuming plane wave propagation, the transfer functions H_I and H_R become $H_I = e^{-jk_z s}$, $H_R = e^{jk_z s}$, with $j = \sqrt{-1}$, with $s = |x_1 - x_2|$ being the distance between microphones and k_z being the wave number in the axial direction. In order to translate the reflection coefficient to the reference surface, defined at $x = 0$, a factor $e^{j2k_z x_1}$ is introduced in (1), leading to the following expression for the normal reflection coefficient

$$\mathcal{R} = \mathcal{R}_1 e^{j2k_z x_1} = \frac{H_{12} - e^{jk_z s}}{e^{jk_z s} - H_{12}} e^{j2k_z x_1}. \tag{2}$$

The normalized specific acoustic impedance Z can be finally obtained by means of

$$Z = \frac{1 + \mathcal{R}}{1 - \mathcal{R}}. \tag{3}$$

Z is usually split in its real R (resistive) and imaginary X (reactive) components, $Z = R + jX$. On the other hand, the specific acoustic impedance Z' will be given by $Z' = Z_0 Z$, Z_0 standing for the characteristic impedance of the medium whose expression is provided in Sec. III B.

B. Problem statement

Suppose that the radiation impedance Z_r or the input impedance Z_{in} of a vocal tract is to be computed from a time domain numerical simulation, using the TMTF method. First, an impedance duct has to be coupled to the reference surface, the duct having the same cross-sectional area and shape than this surface. For instance, to compute the input impedance of a vocal tract, the impedance duct will be coupled to the vocal tract at the glottal cross-section (see Fig. 1), while for the radiation impedance, the duct will be coupled to the mouth exit replacing the existing vocal tract geometry (see Fig. 1).

The next step consists in carrying out a time domain numerical simulation for the acoustic pressure evolution. Let us denote by Ω the finite computational domain with boundary $\partial\Omega$. $\partial\Omega$ is built from five non-intersecting regions, i.e., $\partial\Omega = \Gamma_G \cup \Gamma_Z \cup \Gamma_W \cup \Gamma_H \cup \Gamma_\infty$ with $\Gamma_G \cap \Gamma_Z \cap \Gamma_W \cap \Gamma_H \cap \Gamma_\infty = \emptyset$ (see Fig. 1). Γ_G stands for the impedance duct boundary where a volume velocity is imposed, Γ_Z for the impedance duct walls, Γ_W for the vocal tract walls, Γ_H for the human head boundary, and Γ_∞ for the external boundary, where a fictitious non-reflecting condition has to be imposed. The problem to be solved is that of finding the acoustic pressure field $p(\boldsymbol{x}, t)$ in Ω that satisfies

$$(\partial_{tt}^2 - c_0^2 \nabla^2)\, p(\boldsymbol{x}, t) = 0 \quad \text{in } \Omega,\ t > 0, \tag{4a}$$

with boundary and initial conditions

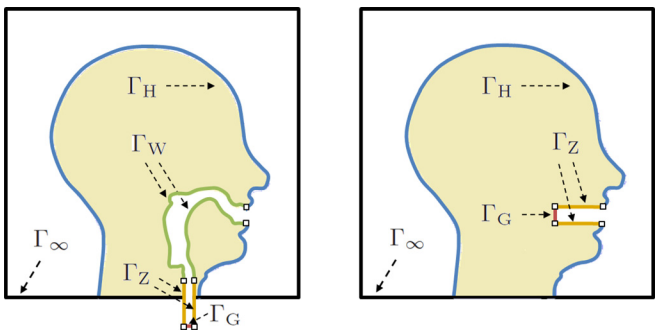

FIG. 1. (Color online) A sketch of the computational domain Ω of Eq. (4) in text for input impedance computations (left) and radiation impedance computations (right). Γ_G stands for the impedance duct boundary where a volume velocity is imposed, Γ_Z for the impedance duct walls, Γ_W for the vocal tract walls, Γ_H for the human head and Γ_∞ for a fictitious non-reflecting boundary that emulates free-field conditions.

$$\nabla p(\boldsymbol{x},t)\cdot\boldsymbol{n} = -\rho_0/S\partial_t Q(t) \quad \text{on } \Gamma_G, t>0, \tag{4b}$$

$$\nabla p(\boldsymbol{x},t)\cdot\boldsymbol{n} = -\mu_w/c_0\partial_t p(\boldsymbol{x},t) \quad \text{on } \Gamma_w, t>0, \tag{4c}$$

$$\nabla p(\boldsymbol{x},t)\cdot\boldsymbol{n} = -\mu_z/c_0\partial_t p(\boldsymbol{x},t) \quad \text{on } \Gamma_z, t>0, \tag{4d}$$

$$\nabla p(\boldsymbol{x},t)\cdot\boldsymbol{n} = 0 \quad \text{on } \Gamma_H, t>0, \tag{4e}$$

$$\nabla p(\boldsymbol{x},t)\cdot\boldsymbol{n} = 1/c_0\partial_t p(\boldsymbol{x},t) \quad \text{on } \Gamma_\infty, t>0, \tag{4f}$$

$$p(\boldsymbol{x},t)=0,\ \partial_t p(\boldsymbol{x},t)=0 \quad \text{in } \Omega,\ t=0. \tag{4g}$$

In Eq. (4), c_0 denotes the speed of sound, ρ_0 the air density, S the impedance duct cross-sectional area at Γ_G, $\partial_t \equiv \partial/\partial t$ designates the partial time derivative, and $\boldsymbol{n}$ the normal vector pointing outwards a surface. With regards to boundary conditions, $Q(t)$ in Eq. (4b) stands for a volume velocity generated by an imaginary loudspeaker. Equations (4c) and (4d) account for constant frequency losses at the inner walls, being μ the boundary admittance coefficient (subindexes w and z simply indicate that different absorption values can be introduced at each boundary). μ is related to the wall impedance Z_w by means of $\mu = \rho_0 c_0/Z_w$. Equation (4e) expresses that the human head is taken as a rigid surface ($\mu = 0$). Finally, Eq. (4f) is the well-known Sommerfeld radiation condition, which guarantees that emanating waves from the mouth propagate outwards to infinity. However, this condition is only optimal for sound waves impinging on Γ_∞ in the normal direction. To overcome this problem, use has been made of a Perfectly Matched Layer (PML) (Berenger, 1994) for the wave equation in its irreducible form. In particular, the PML in Grote and Sim (2010) originally developed for the finite difference framework has been adapted and formulated for our custom finite element code. Details on the implemented numerical scheme can be found in Appendix.

As the simulation evolves, the acoustic pressure signals $p_1(t)$ and $p_2(t)$ are collected at two nodes of the finite element mesh, as if they were virtual microphones. From their Fourier Transform $P_1(f)$ and $P_2(f)$ are obtained and making use of the TMTF method described in Sec. II A, the acoustic impedances can be finally computed.

C. Vocal tract models

The vocal tracts of the three vowels /a/, /i/, and /u/ with circular and elliptical cross-section have been considered. In order to shorten notation, these have been referred as, e.g., circular /a/ or elliptical /a/. For the circular vocal tracts, use has been made of the simplified vocal tract geometries generated from cross-sectional areas provided by Story (2008). With regards to the elliptical vocal tracts (see Fig. 2), the circular cross-sections have been reshaped according to the eccentricity of the elliptical mouth apertures described in Fromkin (1964). A spherical surface of radius 0.09 m has been used to emulate the human head in all cases.

Following the procedure outlined at the beginning of Sec. II B (see Fig. 2), the vocal tract geometry has been replaced by an impedance duct with equal mouth aperture to compute the vocal tract radiation impedance, whereas an impedance duct has been coupled at the glottal cross-section of the vocal tract to compute its input impedance (see Table I for duct dimensions). The impedance duct has a length of $L = 0.1$ m to fulfill the requirements of the standard ISO 10534-2 (1998) (the length should be at least three times the duct radius or the major semi-axis). The virtual microphones have been located at the centerline of the impedance duct and separated a distance $s = 0.01$ m apart (see Fig. 3). Following the recommendations of the ISO 10534-2 (1998), the first virtual microphone has been placed at a distance from the reference surface slightly larger than two times the impedance duct radius, or the major semi-axis. Concerning the reference surface for vocal tract radiation impedances computations, it should be noted that it is well-defined for the circular case given that the intersection of a cylindrical vocal tract with a spherical human head results in a flat disk. However, this is not the case if an elliptical vocal tract is used. In such a case, the elliptical cross-section where the major semi-axis intersects the sphere has been chosen as the reference surface (see Fig. 3).

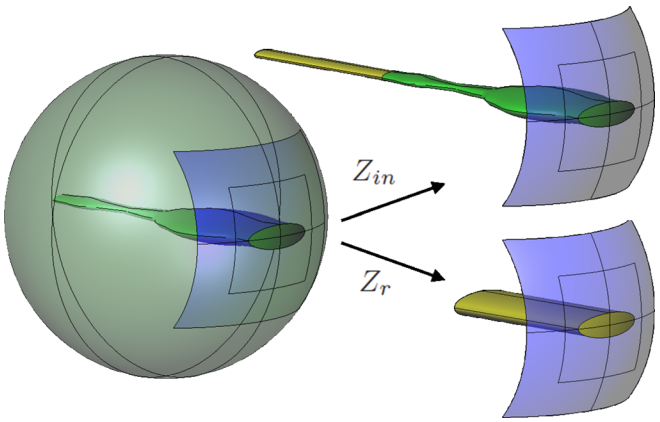

FIG. 2. (Color online) Geometries used for computing (top right) the input impedance and (bottom right) the radiation impedance of (left) the elliptical vowel /a/.

D. Simulation details

The computational domain consists of an outer volume of dimensions $0.25\,\text{m} \times 0.2\,\text{m} \times 0.2\,\text{m}$, where the spherical head has been placed so that sound waves can emanate from the mouth. This volume has been surrounded with a PML of width 0.1 m to absorb any incident wave. The PML has been configured to get a relative reflection coefficient of $r_\infty = 10^{-4}$ (see Appendix). The computational domain has been meshed using unstructured tetrahedral elements with a size comprising $h \approx 0.1$ cm inside the impedance duct, $h \approx 0.5$ cm in the outer volume and $h \approx 0.75$ cm in the PML region (see Fig. 3 to appreciate some mesh details).

TABLE I. Radius a, major semi-axis a_e and minor semi-axis b_e in cm of the circular and elliptical impedance ducts used to compute the radiation impedance Z_r and the input impedance Z_{in} for vowels /a/, /i/, and /u/.

	Z_r/a/	Z_r/i/	Z_r/u/	Z_{in}/a/
a	1.23	0.54	0.23	0.43
a_e/b_e	2.21/0.68	1.25/0.23	0.47/0.11	0.76/0.23

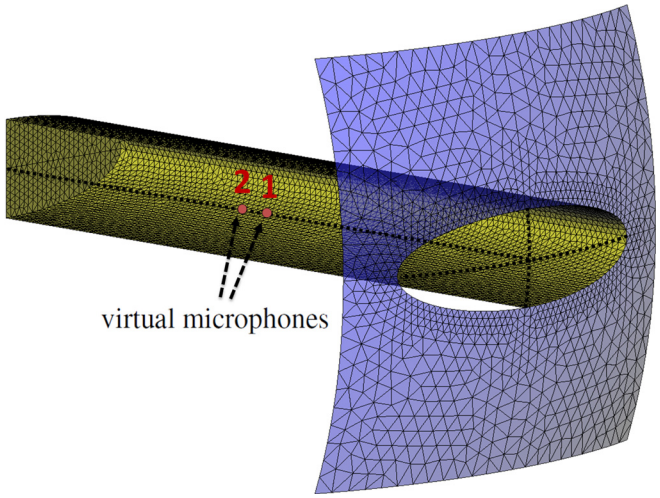

FIG. 3. (Color online) Cut with surface mesh details of the impedance duct for the elliptical /a/ radiation impedance computation. Dots indicate locations of virtual microphones for capturing $P_1(f)$ and $P_2(f)$ in text.

Equation (4) with a PML included has been solved using the finite element approach described in Appendix. A time interval of total duration $T = 30$ ms has been simulated using a sampling rate of $f_s = 1/\Delta t = 2000$ kHz. The values $c_0 = 350$ m/s and $\rho_0 = 1.14$ kg/m^3 have, respectively, been chosen for the speed of sound and for the air density. Concerning boundary conditions, a wideband impulse has been used for the volume velocity $Q(t)$ in Eq. (4b), consisting of a Gaussian pulse of the type (Takemoto *et al.*, 2010)

$$gp(n) = e^{[(\Delta t\, n - T_{gp})0.29 T_{gp}]^2}\,[\mathrm{m}^3/\mathrm{s}], \tag{5}$$

with $T_{gp} = 0.646/f_0$ and $f_0 = 10$ kHz. To avoid numerical errors beyond the maximum frequency of interest ($f_{max} = 10$ kHz), this pulse has been filtered using a low-pass filter with cutoff frequency 10 kHz. For the boundary admittance coefficient at the vocal tract walls the value $\mu_w = 0.005$ has been used, which corresponds to the wall impedance of the vocal tract tissue $Z_w = 83\,666$ kg/m^{2}s (see Švancara and Horáček, 2006). For the impedance duct, the artificial value $\mu_z = 0.01$ has been chosen for the reasons explained in Sec. III.

III. THE TWO-MICROPHONE TRANSFER FUNCTION METHOD FOR NUMERICAL SIMULATIONS

A. Damping the first impedance duct eigenmode

Although theoretically numerical simulations to compute vocal tract impedances could be carried out using a lossless impedance duct, including boundary losses is mandatory for the simulations to have a reasonable duration. From an experimental point of view, time duration is not a problem given that, for example, a measurement that lasts 5 s can be easily performed. However, in the numerical framework the CFL stability condition pose severe restrictions on the time step Δt to be used, so that for intricate and large computational domains, a 5 s event may involve several hours of computational time.

Consider, for example, the radiation impedance computation of the circular /a/ in two cases: (1) a lossless impedance duct with $\mu_z = 0$ and (2) a lossy impedance duct with $\mu_z = 0.01$. Let us first focus on the acoustic pressure collected at the first virtual microphone #1 (see Fig. 3) and plot its time evolution for the lossless and lossy cases in Fig. 4. For the former, the 30 ms duration of the simulation has not sufficed to attenuate the signal acoustic pressure inside the impedance duct, while it has decayed in about 15 ms for the lossy case. It should be remarked that given that the acoustic pressure has to be Fourier transformed to apply the TMTF method, it is necessary for it to vanish to 0 during the simulation interval, to avoid spurious errors in this operation. Some more insight on what is going on inside the impedance duct can be obtained from the spectrograms (time vs frequency) of the acoustic pressure signals for the lossless and lossy cases (see Fig. 5). As observed, the problem arises from the difficulty to attenuate the first duct eigenmode. This is attributed to the fact that radiation is by far a more effective energy dissipating mechanism at high frequencies than at low frequencies. Therefore, the inclusion of wall damping clearly helps to overcome this problem and noticeably shortens the duration of the simulation.

The value $\mu_z = 0.01$ for the impedance duct simulations of vowel /a/ has been deemed appropriate from numerical experiments. It is important to note that μ_z has to be such that the assumption of nearly hard walls is satisfied ($\mu_z \ll 1$). This is necessary to ensure that the mode coupling impedances are negligible (see Sec. III D). Besides, increasing μ_z to reduce the time duration of the computation T lowers the frequency resolution given that $\Delta f = 1/T$. Moreover, if μ_z becomes too large almost no wave is reflected from the duct termination, which results in a very poor estimate for the impedance. For instance, numerical tests with $\mu_z = 0.5$ yielded completely wrong impedances. Finally, it should be remarked that using $\mu_z = 0.01$ also for vowels /i/ and /u/ would be inappropriate. At the end of the following section it will be shown how to modify the admittance coefficient so as to guarantee that propagating waves through /i/ and /u/ impedance ducts experience the same amount of attenuation than in the /a/ duct.

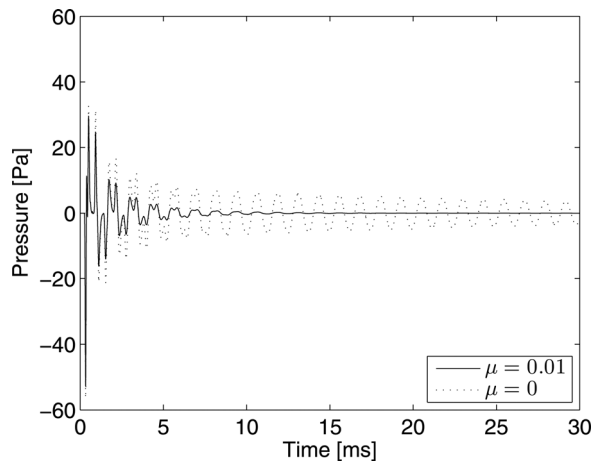

FIG. 4. Acoustic pressure evolution for circular /a/ at virtual microphone #1 for the lossless ($\mu = 0$) and lossy ($\mu = 0.01$) cases.

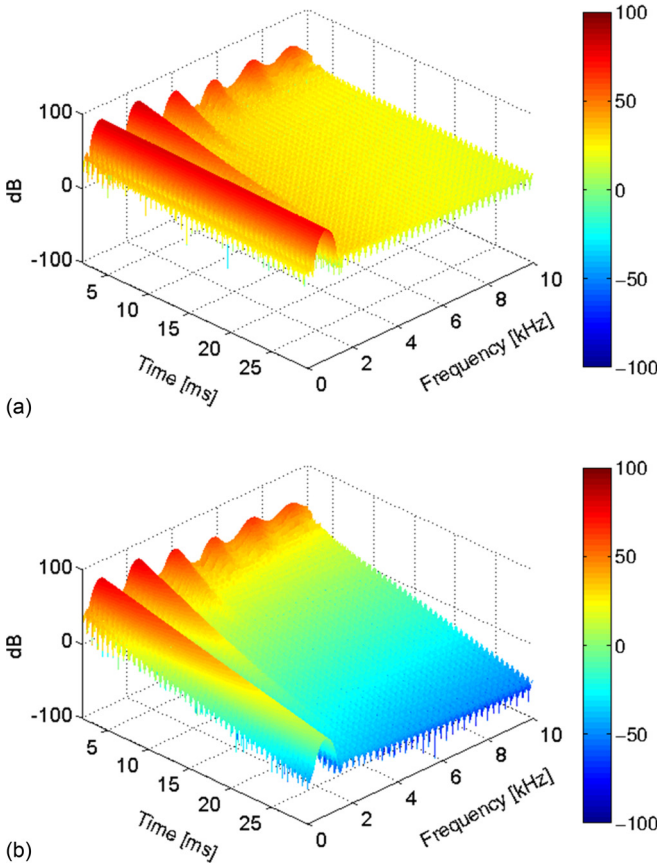

FIG. 5. (Color online) Spectrograms for the acoustic pressures in Fig. 4: (a) lossless impedance duct ($\mu = 0$) and (b) lossy impedance duct ($\mu = 0.01$).

B. Analytical expressions for the complex axial wave number

Introducing artificial damping at the impedance duct walls of the numerical model involves dealing with complex axial wave numbers k_z in expression (2) of the TMTF method. In experimental measurements, a calibration procedure is usually conducted for estimating the attenuation factor (e.g., Boonen *et al.*, 2009). In the numerical case, analytical expressions can be used for k_z. k_z can be related to the admittance boundary coefficient μ_z for a generic duct of arbitrary shape with perimeter $\mathcal{P}$ and cross-section S (see e.g., Sivian, 1937). For illustrative purposes, in what follows such an expression will be derived for the particular case of three-dimensional ducts of elliptical cross-section, though following analogous reasoning lines to those in Munjal (1987) for circular and rectangular ducts.

To proceed, it is convenient to express the wave equation in elliptic cylindrical coordinates (ξ, η, z) (see, e.g., Lowson and Baskaran, 1975). For each constant value of z, the coordinate lines correspond to confocal ellipses and hyperbolae. Curves of constant ξ are ellipses while curves of constant η are hyperbolae. Assuming a harmonic time dependence $\exp(j\omega t)$, so that Eq. (4) transforms to the Helmholtz equation, results in the following expression for the boundary condition Eq. (4d) at the duct wall ($\xi = \xi_0$), in elliptic cylindrical coordinates (see, e.g., Oliveira and Gil, 2010)

$$\frac{\partial \hat{p}}{\partial \xi} + j\mu_z \kappa \sqrt{1 - e^2 \cos^2 \eta}\,\hat{p} = 0 \quad \text{at } \xi = \xi_0. \tag{6}$$

$\hat{p}(\boldsymbol{x}, \omega)$ stands for the time Fourier transform of the sound pressure $p(\boldsymbol{x}, t)$ and $e = \sqrt{1 - b_e^2/a_e^2}$ is the eccentricity of the ellipse defining the duct boundary at ξ_0, which has focal distance $\ell = a_e e$ and major and minor semi-axes $a_e = \ell \cosh \xi_0$ and $b_e = \ell \sinh \xi_0$. $\kappa \equiv k_0 a_e$ is the reduced (adimensional) wave number. To simplify notation, use will be also made of the parameter

$$q \equiv \left(\frac{k_\perp \ell}{2}\right)^2 = \left(\frac{k_\perp a_e e}{2}\right)^2, \tag{7}$$

with $k_\perp \equiv \sqrt{k_0^2 - k_z^2}$ standing for the transverse wave number.

Separation of variables for the Helmholtz equation in elliptic cylindrical coordinates results in the so-called Mathieu radial and angular equations. The solutions need to be 2π periodic in η, which plays the role somehow analogous to θ for the circular case (developed, e.g., in Munjal, 1987, Chap. 1, pp. 35). The periodic solutions are given by products of cosine elliptic functions $ce_m(\eta, q)$, which are even, with the radial Mathieu functions $Je_m(\xi, q)$ related to them, and by sine elliptic functions $se_m(\eta, q)$, which are odd, and their corresponding radial Mathieu functions $Jo_m(\xi, q)$ (see Gutiérrez-Vega, 2000). However, no linear combination of $ce_m(\eta, q)Je_m(\xi, q)$ and $se_m(\eta, q)Jo_m(\xi, q)$ is allowed since the sets of characteristic values for $ce_m(\eta, q)$ and $se_m(\eta, q)$ are different (the situation is somehow similar to what occurs for rectangular ducts, see, e.g., Munjal, 1987, Chap. 1, pp. 28). Given that our interest is in plane wave propagation inside the duct, the lowest modal indices from the even case will have to be considered.

The even radial Mathieu functions $Je_m(\xi, q)$ admit a series factorization in terms of Bessel functions. The factorization depends on m being even or odd which results in even-even $Je_{2k}(\xi, q)$ and even-odd $Je_{2k+1}(\xi, q)$ radial Mathieu function developments. For the case $m = 0$ the former has to be considered. It turns that (Gutiérrez-Vega, 2000)

$$Je_{2k}(\xi, q) = \frac{ce_{2k}(0, q)}{A_0} \sum_{i=0}^{\infty} A_{2i} J_{2i}(2\sqrt{q} \sinh \xi) \tag{8}$$

with J_m corresponding to the Bessel function of order m. Taking $k = i = 0$ yields

$$\hat{p}(\xi, \eta, z) \simeq ce_0(\eta, q) ce_0(0, q) J_0(2\sqrt{q} \sinh \xi), \tag{9}$$

with derivative

$$\frac{\partial \hat{p}(\xi, \eta, z)}{\partial \xi} \simeq -ce_0(\eta, q) ce_0(0, q) \times 2\sqrt{q} \cosh \xi J_1(2\sqrt{q} \sinh \xi). \tag{10}$$

Substituting (9) and (10) into Eq. (6) and evaluating at $\xi = \xi_0$ results in

$$\frac{2\sqrt{q} \cosh \xi_0 J_1(2\sqrt{q} \sinh \xi_0)}{\kappa J_0(2\sqrt{q} \sinh \xi_0)} = j\mu_z \sqrt{1 - e^2 \cos^2 \eta}. \tag{11}$$

Integrating at both sides from 0 to $\pi/2$ allows to eliminate the η dependence in the right hand side of (11). Changing variables to $v=\cos\eta$ shows that the integral in the right hand side is a complete elliptic integral of the second kind, whose solution can be expressed as a series in terms of even powers of the eccentricity (see Abramowitz and Stegun, 1970)

$$\int_0^{\pi/2}\sqrt{1-e^2\cos^2\eta}\,d\eta = \int_0^1 \frac{\sqrt{1-e^2v^2}}{\sqrt{1-v^2}}\,dv = \frac{\pi}{2}\left[1-\sum_{n=1}^{\infty}\left(\frac{(2n-1)!!}{(2n)!!}\right)^2\frac{e^{2n}}{2n-1}\right]\equiv I(e). \quad (12)$$

Using this result, approximating the Bessel functions to first order, $J_0(x)\simeq 1$, $J_1(x)\simeq x/2$, and considering the notation introduced above, it follows from Eq. (11) that

$$q=\frac{j\mu_z\kappa I(e)}{\pi\cosh\xi_0\sinh\xi_0}=j\frac{\mu_z k_0 I(e)a_e^2e^2}{\pi b_e}. \quad (13)$$

From (7) it follows that

$$k_\perp^2=j\frac{4\mu_z k_0 I(e)}{\pi b_e}, \quad (14)$$

and the expected axial wave number becomes

$$k_z=\sqrt{k_0^2-k_\perp^2}\simeq k_0\sqrt{1-j\frac{4\mu_z I(e)}{k_0\pi b_e}}. \quad (15)$$

In the case of zero eccentricity $I(0)=\pi/2$ and $a_e=b_e\equiv a$ so that the axial wave number for the circular case is recovered

$$k_z=\sqrt{k_0^2-k_r^2}\simeq k_0\sqrt{1-j\frac{2\mu_z}{k_0 a}}, \quad (16)$$

which could also be derived from first order approximations in the characteristic equation for circular cylindrical ducts in Munjal (1987), Chap. 1, pp. 36. Given that an ellipse has perimeter $\mathcal{P}=4a_eI(e)$ and surface $S=\pi a_eb_e$ and considering the equivalents for the circle, it follows that Eqs. (15) and (16) are nothing but particular cases of the more general expression

$$k_z\simeq k_0\sqrt{1-j\frac{\mu_z\mathcal{P}}{k_0 S}}. \quad (17)$$

On the other hand, note that to compute the impedance of vocal tracts, impedance ducts of different cross-sections and shapes will be necessary. This implies that the total area of the impedance duct walls will be different in each case, so that if the same boundary admittance coefficient μ_z is used, different internal dissipation would result. To guarantee the same amount of absorption, it must be ensured that the axial wave number remains the same for all cases. Suppose that the same amount of dissipation is wanted for an elliptical impedance duct m than for another elliptical impedance duct n, with respective eccentricities e_m, e_n, and semi-minor axes $b_{e,m}$, $b_{e,n}$. Equating their axial wave numbers (15) it is possible to compute $\mu_{z,m}$ from $\mu_{z,n}$ as

$$\mu_{z,m}=\mu_{z,n}\frac{I(e_n)b_{e,m}}{I(e_m)b_{e,n}}. \quad (18)$$

As mentioned in Sec. III A, in this work a boundary admittance coefficient of $\mu_z=0.01$ has been chosen for the circular vowel /a/. Therefore, to introduce the same amount of dissipation in all simulations, use has been made of (18), with $n=$/a/ and $m=$/i/,/u/.

Finally, using the complex axial wave number derived in (17), the characteristic impedance Z_0 in the impedance duct can be readily obtained from the ratio between the pressure and particle velocity in a lossy duct without mean flow in Munjal (1987), Chap. 6, pp. 232,

$$Z_0=\rho_0c_0\frac{k_0}{k_z}\simeq\rho_0c_0\left(1-j\frac{\mu_z\mathcal{P}}{k_0S}\right)^{-1/2}. \quad (19)$$

For large ducts with small wall losses the usual value $Z_0\approx\rho_0c_0$ is recovered (see, e.g., Dalmont *et al.*, 2001).

C. Accuracy of complex axial wave numbers

Several assumptions have been made in order to derive the axial complex wave numbers in (15) and (16). Let us next check if these simple expressions are precise enough for vocal tract impedance computations and what would happen if real wave numbers were considered instead. To do so, the radiation impedance of the circular and elliptical /i/ using complex and real wave numbers have been computed considering different pairs of virtual microphones, located at different distances from the duct exit. The computed radiation impedances, splitted in terms of resistance R_r and reactance X_r, have been plotted in Fig. 6 and compared to the theoretical model of the baffle set in a spherical surface (Morse and Ingard, 1968, Chap. 7, pp. 343), for the circular case. The single point arrow on the R_r curves indicates their tendency when the selected pairs of microphones used for the computations are moved away from the duct exit (see duct scheme in the upper left side of figures). The double point arrow indicates that the X_r curves do not follow any clear tendency when changing the pairs of virtual microphones.

Having a look at Eq. (2), it can be observed that the term $e^{j2k_zx_1}$ is used to translate the reflection coefficient R_1 to the reference plane (x_1 is the distance from the first virtual microphone to the reference plane). Taking into account the first order approximation $(1+x)^{1/2}\sim 1+x/2$ in the expression for the complex wave number in (15) (which is valid for hard wall behavior $|Z_w|\gg\rho_0c_0$), it follows that $k_{z,00}\equiv k_z\simeq k_0-j2\mu_zI(e)/(\pi b_e)$. Substituting into the propagator $e^{j2k_zx_1}$ results in $e^{j2x_1k_0}e^{j2x_1\mu_zI(e)/(\pi b_e)}$, so that the factor $e^{j2x_1\mu_zI(e)/(\pi b_e)}$ will be missing if a real wave number is used. Note that the higher the value of x_1 the larger will be the error. This can be appreciated in Fig. 6(a) for the circular case, where R_r clearly departs from the theoretical curve as x_1 increases. As

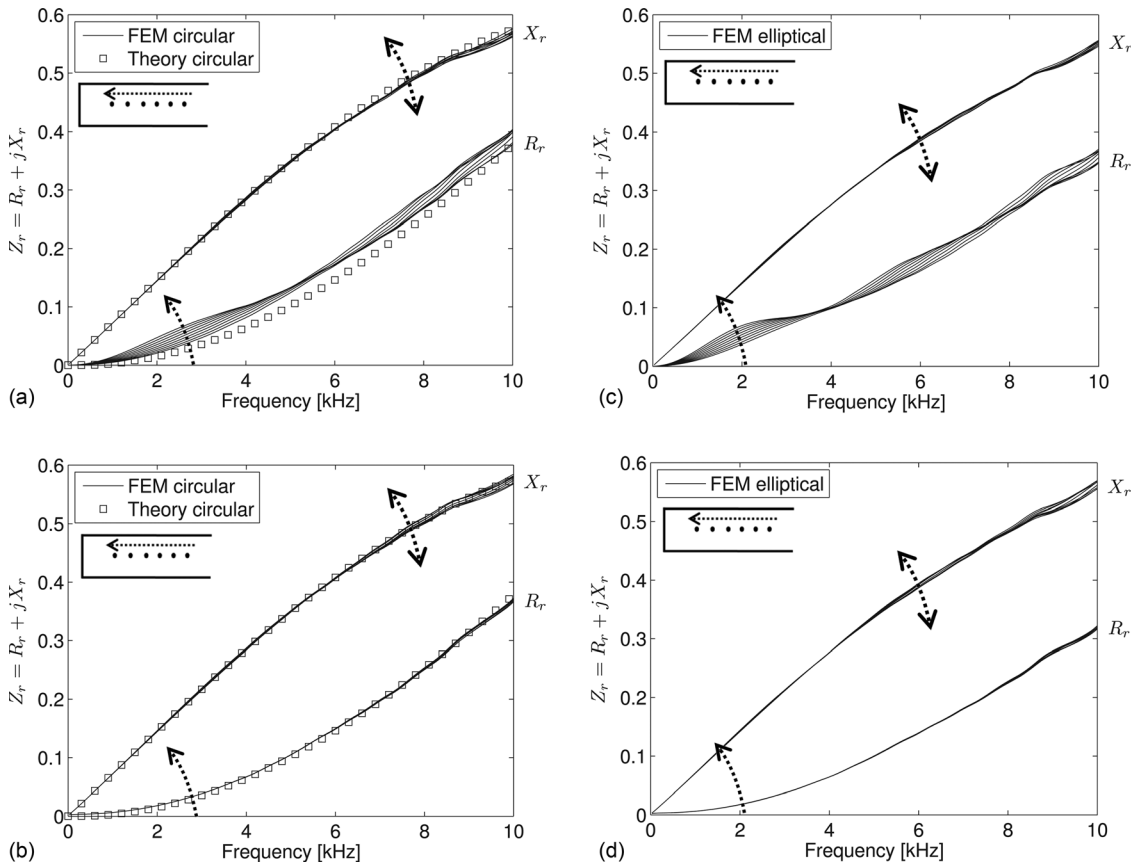

FIG. 6. Radiation resistance R_r and reactance X_r for vowel /i/ with circular (top) and elliptical (bottom) mouth aperture for different pairs of virtual microphones. (a) and (c) Real wave number computations. (b) and (d) Complex wave number computations. Solid lines correspond to FEM simulations and square symbols to the theoretical model, only available for a circular piston.

opposite, the error is inexistent when the appropriate complex wave number of Eq. (16) is used in (2), and the computed curve perfectly matches the theoretical one [see Fig. 6(b)]. The reactance X_r seems not to be as much affected as the resistance R_r by the error.

A very similar behavior can be observed for the elliptical case as shown in Fig. 6(c) and Fig. 6(d). Besides, note that both for the circular and elliptical cases, some discrepancies are found for the reactance values at the high frequency range, even when using the correct complex wave numbers. This is attributed to numerical errors in the simulations to be discussed in Sec. III E.

D. Plane wave propagation restriction

At this point, it is convenient to comment that by using the TMTF method described in this work only the direct impedance of the planar wave mode can be computed. This is the one that dominates below the first cutoff frequency f_c of the impedance duct. However, above f_c, higher order modes get excited and combine with the planar one resulting in complicated pressure patterns inside the duct (see, e.g., Motoki, 2002). To capture this acoustic multi-modal behavior, a direct impedance is required for each mode, leading to a matrix representation of the impedance, as described in Zorumski (1973). Coupling between modes may also occur and perturb the direct impedances. This effect is quantified by the coupling impedances and can be neglected for nearly hard walls (see Morfey, 1969; cf. Zorumski, 1973). This is the case for vocal tract acoustics given that the values $\mu_w = 0.005$ and $\mu_z = 0.01$ have respectively been used for the vocal tract walls and for the impedance duct walls, as detailed in the preceding sections.

Although high order modes direct impedances are needed for an accurate characterization of the radiation impedance above f_c, several theoretical models such as the piston set in a spherical baffle, which only consider the direct impedance of the plane wave propagation, are still used in 3D simulations to emulate radiation (e.g., Zhou *et al.*, 2008; Vampola *et al.*, 2008). This is so because the computational domain (and hence the time duration of the simulation) can be strongly reduced given that no radiation space is required. Therefore, it would be interesting to use the TMTF method for computing the planar mode direct impedance above f_c, to allow comparison with those theoretical models. It will be next shown how this can be done through appropriate location of the virtual microphones inside the duct.

For a circular impedance duct of radius a, the first non-planar eigenmode is the (1,0) mode, with a cutoff frequency $f_{(1,0)} = 1.84c_0/(2\pi a)$ (Fletcher and Rossing, 1988). The next one, is the (2,0) mode, with $f_{(2,0)} = 3.05c_0/(2\pi a)$, followed by the (0,1) mode, with $f_{(0,1)} = 3.80c_0/(2\pi a)$. In the experimental framework, the (1,0) mode limits the working frequency range of the TMTF method. However, in the numerical framework, this limitation can be overcome by a proper location of the virtual microphones. Having a look at the

pressure distribution of the first three eigenmodes [see Fig. 7(a)], nodal planes can be observed (corresponding to lines in the duct cross-sections of the figure), which cross the centerline of the duct for the (1,0) and (2,0) modes. Consequently, locating the virtual microphones at the centerline will avoid the pressure there being unaffected by these modes. The TMTF method will be then still applicable at these frequencies and limited by the (0,1) mode, which is the first eigenmode that does not have a nodal line at the center of the duct [see Fig. 7(a)].

With regards to elliptical ducts, the frequency range can also be extended. In Fig. 7(b) the pressure patterns of the first four eigenmodes are presented for the elliptical /a/ impedance duct (these can be computed, e.g., from the formulas in Oliveira and Gil, 2010). The first non-planar mode is the even mode (1,1). This mode has a nodal plane in the center, so that locating again the virtual microphones in the centerline of the impedance duct will allow to extend the analysis up to the frequency of the even mode (2,1), which is the limiting one in this case.

The first modes of the impedance ducts used in this work are shown in Table II, with superscript a denoting in each case the first mode without a nodal plane at its center (i.e., the limiting one). As expected, the impedance duct with a strongest restriction is that of vowel /a/ (largest mouth aperture), whereas vowel /u/ (smallest mouth aperture) presents the less stringent condition. It can also be observed that working with elliptical mouth apertures results in more restrictive frequency ranges. Note however that by locating the virtual microphones at the centerline of the impedance duct, the upper frequency limit of the experimental TMTF method has been almost increased by a factor ~2. Except for the elliptical /a/, the desired frequency range of analysis that goes up to $f_{max} = 10$ kHz can thus be attained.

E. The singularity of the TMTF method

It is well-known that a singularity occurs in the experimental TMTF method when half the wavelength of the acoustic pressure equals the microphone spacing s, or one of its multiples. The minimum frequency that satisfies this condition is termed the *critical frequency*, $f_{cr} = c_0/(2s)$, and imposes a high frequency limit $f_u < f_{cr}$ to the method. On the other hand, a minimum low frequency limit f_d also exists,

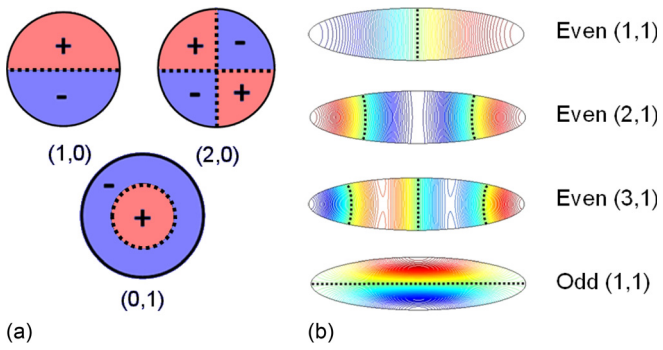

FIG. 7. (Color online) Plots of the lower standing modes in an impedance duct with (a) circular and (b) elliptical cross-section. Discontinuous lines represent nodal planes.

TABLE II. Frequency values in kHz for the first eigenmodes of the circular and elliptical impedance ducts used to compute the radiation impedance Z_r and the input impedance Z_{in} for vowels /a/, /i/ and /u/.

		Circular			Elliptical			
		(1,0)	(2,0)	(0,1)	E(1,1)	E(2,1)	E(3,1)	O(1,1)
Z_r	/a/	8.33	13.81	17.2[a]	4.68	8.6[a]	12.47	13.79
	/i/	19.05	31.58	39.35[a]	8.27	15.27[a]	22.18	39.3
	/u/	45.42	75.28	93.8[a]	22.23	40.98[a]	59.49	84.2
Z_{in}	/a/	24.07	39.89	49.7[a]	13.57	24.97[a]	36.2	40.03

[a]Maximum frequency of analysis when the virtual microphones are located at the centerline of the impedance duct.

because the pressure differences measured by the two microphones will be negligible if their distance apart is very small compared to the measured wavelength. Working close to both limits is not recommended, and a suitable option is to take $f_d = 0.2 f_{cr} < f < 0.8 f_{cr} = f_u$ (as proposed in Jang and Ih, 1998).

The above situation contrasts with that of numerical simulations. Suppose that a simulation up to a given frequency f_{max}, with corresponding wavelength λ_{min}, is to be carried out. In the case of unlimited computational resources at disposition, a fine enough mesh could be used to meet the standard criterion of ten nodes per wavelength for λ_{min} (see, e.g., Ihlenburg, 1998) and numerical errors would be negligible. In such situation the only frequency upper limitation would come from the plane wave restriction discussed in Sec. III D, so it would be reasonable to take, e.g., $f_d = 0 < f < f_{max} = f_{cr} = f_u$ as the operational working frequency range. This expression together with $f_{cr} = c_0/(2s)$ provides the following possible values for the virtual microphone spacing s

$$h \leq s < 0.5\lambda_{\min}. \tag{20}$$

Note from (20), that obviously the microphone spacing s cannot be smaller than the mesh size h.

However, working with very fine meshes can be unfeasible in many simulations, and the ten nodes per wavelength criterion is often sacrificed to lower the computational cost. This results in the appearance of some numerical errors at high frequencies as happens with the simulations performed throughout this work, where 34.5, 6.9, and 4.6 nodes per λ_{min} have been respectively taken within the impedance duct, the outer volume and the PML region (see Sec. II D for mesh details). In Fig. 8 plots of the radiation resistance and reactance for the elliptical /i/ are given, computed using different microphone spacings, $s = 0.1$, 0.25, 0.5, 0.75, 1, 1.25, and 1.5 cm, which yield $s/\lambda_{min} \sim 0.03$, 0.07, 0.15, 0.22, 0.29, 0.36, and 0.43, respectively. The first spacing ($s = 0.1$ cm) has been chosen equal to the mesh size h inside the impedance duct (dashed curve in Fig. 8), while the last one ($s = 1.5$ cm) has a value close to the singularity value $0.5\lambda_{min}$ (dotted curve in Fig. 8). No differences can be appreciated in Fig. 8 between the various R_r and X_r curves for the low-mid frequency range as there are no significant numerical errors at these frequencies for the present simulations. Slight

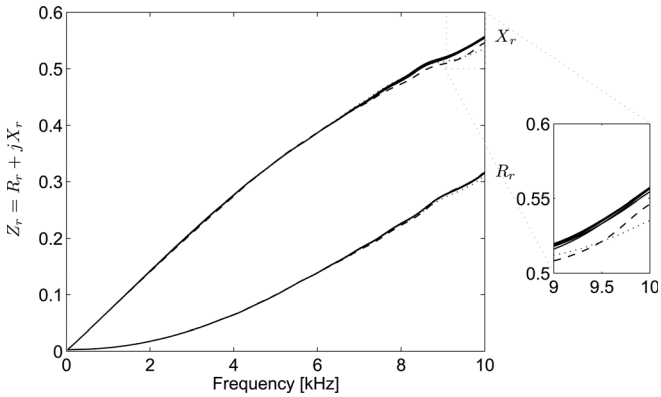

FIG. 8. Resistance and reactance of the elliptical /i/ for different microphone spacings s. The dashed line stands for $s = 0.1$ cm (equal to the mesh size h), the dotted line for $s = 1.5$ cm (close to the singularity), and solid lines correspond to intermediate values of s.

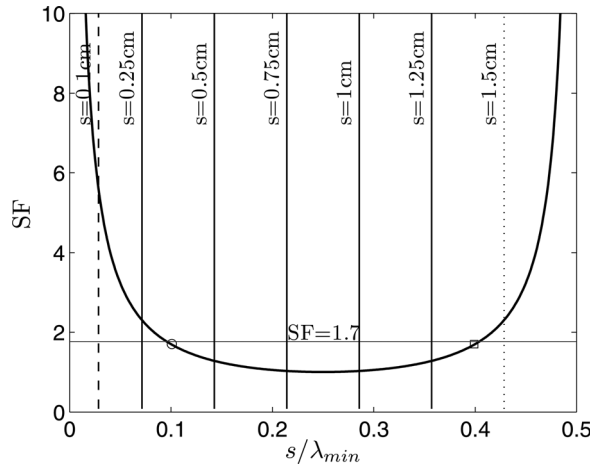

FIG. 9. Singularity factor SF of the TMTF method for a lossless impedance duct. The circle and the square denote the low and high limits for the microphone spacing s obtained when SF = 1.7. Vertical lines correspond to the microphone spacing configurations used in the example of Fig. 8.

differences only become apparent for frequencies higher than 8 kHz (see zoom in Fig. 8), the largest ones precisely corresponding to the reactances computed with the limiting values of $s = 0.1$ cm (mesh size) and $s = 1.5$ cm (singularity value).

The above example shows that the condition in Eq. (20) for the microphone spacing is too loose and that stronger requirements are needed in practice for the spacing limiting values. In order to define them, resort is made to the so called singularity factor (SF) of the TMTF method, introduced by Jang and Ih (1998). The SF indicates the sensitivity of the TMTF method to errors in the input pressures $P_1(f)$ and $P_2(f)$; the higher the SF value the stronger the influence of the error sources in the computed impedances. When computing the SF in the experimental framework, it is assumed that all errors are of the white type, uncorrelated, and with constant variance. This will not be the case of a single numerical simulation, the error being totally deterministic, i.e., always the same if the computation becomes reran. However, considering the simulation of a given vocal tract impedance being representative of a certain ensemble average of vocal tracts having, e.g., slight different geometry details and material characteristics, it is reasonable to hypothesize that errors arising from these simulations would satisfy the error requirements for the SF computation. It would then be logical to demand that the chosen spacing for the virtual microphones results in a small SF value.

In Fig. 9, the SF curve (thick line) for the standard TMTF method in a lossless impedance duct (implementation of the SF for a lossy impedance duct is out of the scope of this work) has been plotted according to the procedure described in Jang and Ih (1998). However, instead of representing the SF dependence with frequency, this has been plotted versus the microphone spacing s (normalized by λ_{min}). Moreover, the microphone spacings corresponding to the resistance and reactance curves in Fig. 8 have been also plotted as vertical lines. As observed in the figure, the SF values for the extreme spacings corresponding to the mesh size and singularity values are much higher than the threshold value of SF ≤ 1.7, recommended in the experimental framework (see Jang and Ih, 1998). According to this criterion a more restrictive range is obtained for the virtual microphone spacing than that provided by Eq. (20), namely,

$$h < 0.1\lambda_{min} < s < 0.4\lambda_{min}. \tag{21}$$

The optimum, and thus recommended, spacing s will be that minimizing SF, which is close to $s \simeq 0.25\lambda_{min}$ in Fig. 9. In the computations $s = 1$ cm has been used (see Sec. II D) that yields $s \simeq 0.29\lambda_{min}$.

IV. VOCAL TRACT IMPEDANCES

In this section, radiation and input impedances for vowel vocal tracts using the described FEM-TMTF approach will be presented. As detailed in Sec. II, the radiation impedance for vowels /a/, /i/, and /u/ has been computed considering circular and elliptical mouth apertures, as well as the input impedance of vowel /a/ for circular and elliptical vocal tracts.

In Fig. 10 the results for the radiation impedance are given, split in terms of the radiation resistance [Fig. 10(a)] and reactance [Fig. 10(b)]. All results are provided up to 10 kHz except for the elliptical /a/, the analysis only being valid in this case up to ~8 kHz because of the limiting even mode (2,1) ($f = 8.6$ kHz, see Table II). Note, however, that this value can be reached thanks to proper location of the virtual microphones (see Sec. III D) and that the experimental TMTF would have only let to measure impedance values up to $f = 4.68$ kHz, corresponding to the even mode (1,1) (see Table II). Similarly, the plane wave frequency restrictions for the circular /a/ ($f = 8.33$ kHz) and for the elliptical /i/ ($f = 8.27$ kHz) in the experimental TMTF, can be easily overcome thanks to centerline microphone positioning. Thus, for all analyzed cases, except for the elliptical /a/, the radiation impedance can be computed for the whole frequency range of interest (0 10] kHz, without problems (see Table II).

The differences between the resistance and reactance curves for the circular and elliptical mouth apertures in Fig. 10 can be justified as follows (remember that for a given

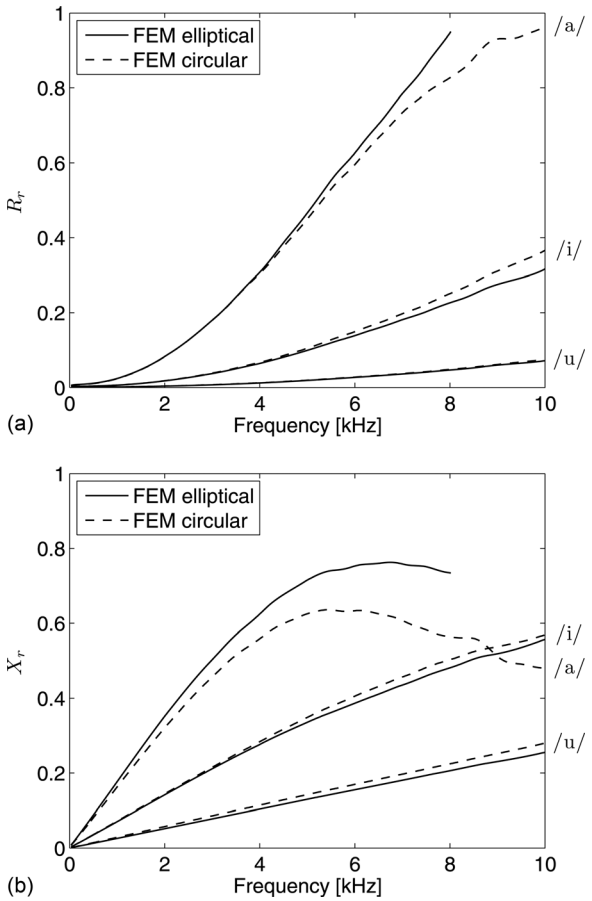

FIG. 10. (a) Radiation resistance and (b) reactance for the elliptical and circular vocal tracts of vowels /a/, /i/, and /u/.

vowel only the shape of the mouth, elliptical or circular, changes but not the total mouth surface).

In the plane wave propagation regime, the curves should be almost identical. However, as explained in Sec. II D, the reference surface for elliptical mouth apertures is defined at the intersection between the major semi-axis of the impedance duct with the sphere. This implies that there is a small partial protrusion of the duct beyond the reference surface, which reaches the intersection between the minor semi-axis and the sphere, and plays somehow the role of some kind of lips. Its effects on the radiation impedance of the elliptical ducts can be understood as those of a modified end correction. To first order approximation, when $R_r^2 + X_r^2 \ll 1$, the inertial end correction only affects the reactance. This is what can be observed for vowel /u/, which shows the same resistance values for the circular and elliptical cases [see Fig. 10(a)], but different ones for the reactance [see Fig. 10(b)]. For vowels /a/ and /i/ the condition $R_r^2 + X_r^2 \ll 1$ is no longer satisfied, say for frequencies bigger than 4 kHz, and differences in resistance values can become more clearly appreciated.

Finally, moduli results for the input impedance of the circular and elliptical /a/ are plotted in Fig. 11 (results for vowels /i/ and /u/ have not been included as very similar conclusions to those of /a/ could be deemed). In contrast to the radiation impedance computation, the input impedance for elliptical /a/ can be computed with no problem up to 10 kHz. This is because the glottal cross-section is much

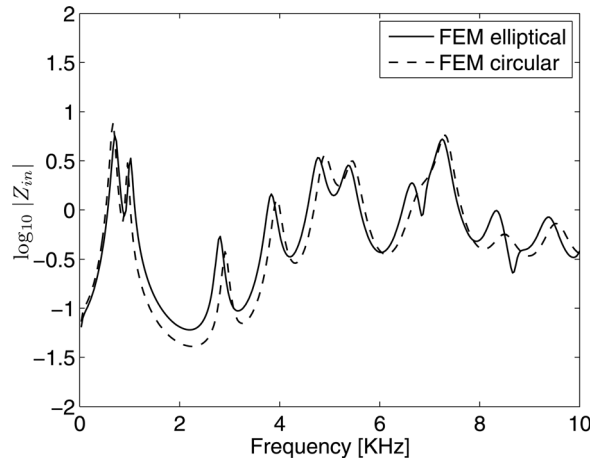

FIG. 11. Input impedance for the circular and elliptical /a/.

smaller than the mouth aperture; a narrower impedance duct is then required, which will have the first non-planar mode beyond 10 kHz. Looking at Fig. 11, it can be observed that below 5 kHz the input impedance moduli of the circular and elliptical /a/ are very similar indicating that they are both in the plane wave propagation range. Note, however, that there is a certain formant shift to lower frequencies for the elliptical /a/ because its radiation reactance is higher than that of the circular /a/ [see Fig. 10(b)]. Above 5 kHz, differences become notorious due to non-planar high order mode effects.

V. CONCLUSIONS

The radiation and input impedances of vowel vocal tracts, with circular and elliptical cross-sections, have been computed using an adaptation of a TMTF experimental method to a numerical framework. The procedure is rather straightforward and does not require any computation of the acoustic velocity field; though in return, it demands an additional simulation with an impedance duct to obtain radiation impedances. Despite the simplicity of the method, some considerations are to be taken into account. First, it has been shown that it is mandatory to impose losses at the impedance duct walls to attenuate the first duct eigenmode and achieve reasonable computational times. This implies using complex wave numbers in the TMTF expressions, which have been derived for three-dimensional cylindrical impedance ducts with elliptical cross-section. Second, the frequency range of validity of the experimental TMTF method can be almost doubled by locating the virtual microphones at the impedance duct centerline. This allows computing of the direct impedance for plane wave propagation above the experimental limitation. Third, a range of possible values for the virtual microphone spacing has been proposed making use of the so called singularity factor. An optimum value of a quarter wavelength of the maximum frequency to be solved has been recommended.

ACKNOWLEDGMENTS

The authors greatly acknowledge Dr. Ramon Codina for providing us with an initial FEM code for the scalar

convection-diffusion-reaction equation from which the actual one has evolved and Dr. Francesc Alías for fruitful discussions and information on several topics related to speech synthesis. This research has been partially supported by EU-FET grant EUNISON 308874. The first author would also like to acknowledge the Generalitat de Catalunya (SUR/ECO) for the pre-doctoral FI Grant No. 2012FI_B 00727.

APPENDIX: TIME DOMAIN FEM APPROACH

This appendix includes the details of the time domain FEM approach used to solve Eq. (4) in Sec. I. This consists in extending the finite difference PML formulation for the irreducible wave equation in Grote and Sim (2010), to the FEM framework.

Replacing the Sommerfeld radiation condition with the PML, the original acoustic wave equation in (4) becomes modified to

$$\partial_{tt}^2 p - c_0^2 \nabla^2 p = \nabla \cdot \phi - \alpha \partial_t p - \beta p - \gamma \psi, \tag{A1a}$$

$$\partial_t \phi_i = -\xi_i \phi_i + c_0^2 a_i \partial_i p + c_0^2 b_i \partial_i \psi, \ \forall i = 1,2,3, \tag{A1b}$$

$$\partial_t \psi = p, \tag{A1c}$$

in Ω, $t > 0$, with boundary and initial conditions

$$\nabla p \cdot \boldsymbol{n} = -\rho_0 / S \partial_t Q \equiv g \quad \text{on } \Gamma_G, t > 0, \tag{A1d}$$

$$\nabla p \cdot \boldsymbol{n} = -\mu / c_0 \partial_t p \quad \text{on } \Gamma_w, t > 0, \tag{A1e}$$

$$\nabla p \cdot \boldsymbol{n} = 0 \quad \text{on } \Gamma_H, t > 0, \tag{A1f}$$

$$\nabla p \cdot \boldsymbol{n} = 0 \quad \text{on } \Gamma_\infty, t > 0, \tag{A1g}$$

$$p = 0, \ \partial_t p = 0 \quad \text{in } \Omega, t > 0, \tag{A1h}$$

$$\phi_i = 0, \ \partial_t \phi_i = 0, \ \forall i = 1,2,3 \quad \text{in } \Omega, t = 0, \tag{A1i}$$

$$\psi = 0, \ \partial_t \psi = 0 \quad \text{in } \Omega, t = 0. \tag{A1j}$$

Note that (A1a) modifies the right hand side of (4a) with the inclusion of some extra terms involving the auxiliary functions ψ and $\boldsymbol{\phi} = (\phi_1, \phi_2, \phi_3)$. Moreover, four additional scalar equations (A1b) and (A1c) are needed for these additional functions. In what concerns the coefficients α, β, γ, a_i, b_i in (A1), they depend on the damping profiles ξ_i and are given by $\alpha = \xi_1 + \xi_2 + \xi_3$, $\beta = \xi_1\xi_2 + \xi_2\xi_3 + \xi_3\xi_1$, $\gamma = \xi_1\xi_2\xi_3$, $a_1 = \xi_2 + \xi_3 - \xi_1$, $a_2 = \xi_3 + \xi_1 - \xi_2$, $a_3 = \xi_1 + \xi_2 - \xi_3$, $b_1 = \xi_2\xi_3$, $b_2 = \xi_3\xi_1$ and $b_3 = \xi_1\xi_2$. The damping profiles ξ_i are used to control the amount of absorption in the PML and many options exist for them. Following Grote and Sim (2010), use has been made of

$$\xi_i(x_i) = \hat{\xi}_i \left[\frac{|x_i - l_i|}{L_i} - \frac{\sin\left(\frac{2\pi |x_i - l_i|}{L_i}\right)}{2\pi} \right], \tag{A2}$$

for $l_i \le |x_i| \le l_i + L_i$. $\hat{\xi}_i$ is a constant accounting for the damping effect in the ith direction, l_i is the ith coordinate of the PML layer and L_i the thickness of the PML region in the ith direction. The constant $\hat{\xi}_i$ depends on the discretization and thickness of the layer and can be computed as

$$\hat{\xi}_i = \frac{c_0}{L_i} \log\left(\frac{1}{r_\infty}\right), \tag{A3}$$

with r_∞ standing for the relative reflection at the boundary of the PML. The PML boundary can be truncated using either a Dirichlet or a Neumann homogeneous condition [the latter has been our choice, see (A1g)]. On the other hand, notice that for $l_i \le |x_i|$, $\xi_i(x_i) = 0$, i.e., outside the PML, the damping profiles ξ_i vanish. In this case, the modified PML wave equation (A1a) reduces to the standard wave equation in (4a).

The set of partial differential equations (A1a)–(A1c) supplemented with boundary and initial conditions (A1d)–(A1j) constitutes the problem to be solved. If a FEM approach is to be used to find a numerical solution for (A1), first the problem has to be set in its weak or variational form. As usual, this is done by first multiplying (A1) by test functions q, v_i, w (q for the pressure, v_i for the first auxiliary functions ϕ_i, and w for the second auxiliary function ψ) and integrating over the computational domain Ω. Applying the divergence theorem and making use of boundary conditions, the weak form of the problem is obtained, which consists in finding p, ϕ_i, and ψ such that

$$\begin{aligned}(q, \partial_{tt}^2 p) + c_0 (q, \mu \partial_t p)_{\Gamma_w} + c_0^2 (\nabla q, \nabla p) \\ = c_0^2 (q, g)_{\Gamma_G} + \sum_{i=1}^{3} (q, \partial_i \phi_i) - (q, \alpha \partial_t p) \\ - (q, \beta p) - (q, \gamma \psi),\end{aligned} \tag{A4a}$$

$$\begin{aligned}(v_i, \partial_t \phi_i) = (v_i, \xi_i \phi_i) + c_0^2 (v_i, a_i \partial_i p) \\ + c_0^2 (v_i, b_i \partial_i \psi), \forall_i = 1,2,3,\end{aligned} \tag{A4b}$$

$$(w, \partial_t \psi) = (w, p), \tag{A4c}$$

in Ω, $t > 0$, with initial conditions

$$(q, p) = 0, \ (q, \partial_t p) = 0, \tag{A4d}$$

$$(v_i, \phi_i) = 0, \ (v_i, \partial_t \phi_i) = 0, \ \forall i = 1,2,3, \tag{A4e}$$

$$(w, \psi) = 0, \ (w, \partial_t \psi) = 0, \tag{A4f}$$

in Ω, $t = 0$, for all q, v_i, w. To shorten notation, in (A4) the integral of the product of any two functions f, g in Ω has been written as

$$(f, g) := \int_\Omega f g d\Omega, \tag{A5}$$

while integrals over boundaries have been explicitly indicated, e.g., $(f, g)_{\Gamma_G}$.

To find a numerical solution to problem (A4), this has to be discretized in both space and time. Let us first discretize it in space using a FEM formulation. Given a finite element partition of Ω with n_{el} elements and n_p nodes and discretizing problem (A4) following the Galerkin method, the

discrete versions of the unknowns p, ϕ_i, ψ and the discrete versions of the test functions q, v_i, and w have been expanded in terms of piecewise linear shape functions $N(\boldsymbol{x})$ (e.g., $p_h = \sum_{b=1}^{n_p} N^b P^b$), which results in the following time evolving algebraic matrix system

$$\boldsymbol{M}\ddot{\boldsymbol{P}} + c_0\boldsymbol{B}\dot{\boldsymbol{P}} + c_0^2\boldsymbol{K}\boldsymbol{P} = c_0^2\boldsymbol{L} + \sum_{i=1}^{3}\boldsymbol{B}_i\boldsymbol{\Phi}_i - \boldsymbol{M}_\alpha\dot{\boldsymbol{P}} - \boldsymbol{M}_\beta\boldsymbol{P} - \boldsymbol{M}_\gamma\boldsymbol{\Psi}, \tag{A6a}$$

$$\boldsymbol{M}\dot{\boldsymbol{\Phi}}_i = -\boldsymbol{M}_{\xi i}\boldsymbol{\Phi}_i + c_0^2\boldsymbol{B}_{\mathrm{i},a_i}\boldsymbol{P} + c_0^2\boldsymbol{B}_{\mathrm{i},b_i}\boldsymbol{\Psi}, \quad \forall i = 1,2,3, \tag{A6b}$$

$$\dot{\boldsymbol{\Psi}} = \boldsymbol{P}, \tag{A6c}$$

in Ω, $t > 0$, with initial conditions

$$\boldsymbol{P} = 0,\ \dot{\boldsymbol{P}} = 0, \tag{A6d}$$

$$\boldsymbol{\Phi}_i = 0,\ \dot{\boldsymbol{\Phi}}_i = 0,\ \forall i = 1,2,3, \tag{A6e}$$

$$\boldsymbol{\Psi} = 0,\ \dot{\boldsymbol{\Psi}} = 0, \tag{A6f}$$

in Ω, $t = 0$. In (A6), $\boldsymbol{P}$, $\boldsymbol{\Phi}_i$, and $\boldsymbol{\Psi}$ stand for the vectors of nodal values that respectively correspond to the pressure and auxiliary functions [e.g., $\boldsymbol{P} = (P^1 \cdots P^{n_p})^\tau$], whereas the remaining matrix and vector entries are given by

$$M^{ab} = (N^a, N^b), \quad M_\alpha^{ab} = (N^a, \alpha_h N^b), \tag{A7a}$$

$$M_\beta^{ab} = (N^a, \beta_h N^b), \quad M_\gamma^{ab} = (N^a, \gamma_h N^b), \tag{A7b}$$

$$M_{\xi_i}^{ab} = (N^a, \xi_{ih} N^b), \quad B^{ab} = (N^a, \mu N^b)_{\Gamma_w}, \tag{A7c}$$

$$B_{i,a_i}^{ab} = (N^a, a_{ih}\partial_i N^b), \quad B_{i,}^{ab} = (N^a, \partial_i N^b), \tag{A7d}$$

$$B_{i,b_i}^{ab} = (N^a, b_{ih}\partial_i N^b), \quad K^{ab} = (\nabla N^a, \nabla N^b), \tag{A7e}$$

$$L^a = (N^a, g)_{\Gamma_G}. \tag{A7f}$$

As usual, the domain integrals in (A7) are to be understood as the summation of integrals over elements Ω_e, i.e., $(\cdot\,,\cdot)_\Omega = \sum_{e=1}^{n_{el}} (\cdot\,,\cdot)_{\Omega_e}$. The subscripts h denote the discrete versions of the corresponding continuous variables.

Let us next proceed to the time discretization of (A6). A finite difference approach has been used to do so. Considering a constant time step ($\Delta t = t^{n+1} - t^n$) discretization of the time interval $(0,\ T)$ into $0 < t^1 < \cdots < t^{n-1} < t^n < t^{n+1} < \cdots < t^N \equiv T$. A second order finite difference central scheme has then been implemented for the pressure time derivatives, while a first order central scheme has been used for the time derivatives of the auxiliary variables in the PML region. This is because first order schemes are known to introduce strong numerical dissipation, which in this case is advantageous to help absorbing the waves crossing the PML.

Inserting these time derivative approximations in (A6) yields

$$\boldsymbol{M}\frac{\boldsymbol{P}^{n+1} - 2\boldsymbol{P}^n + \boldsymbol{P}^{n-1}}{\Delta t^2} + c_0\boldsymbol{B}\frac{\boldsymbol{P}^{n+1} - \boldsymbol{P}^{n-1}}{2\Delta t} + c_0^2\boldsymbol{K}\boldsymbol{P}^n = c_0^2\boldsymbol{L}^n + \sum_{i=1}^{3}\boldsymbol{B}_i\boldsymbol{\Phi}_i^n - \boldsymbol{M}_\alpha\frac{\boldsymbol{P}^{n+1} - \boldsymbol{P}^{n-1}}{2\Delta t} - \boldsymbol{M}_\beta\boldsymbol{P}^n - \boldsymbol{M}_\gamma\frac{\boldsymbol{\Psi}^{n+1/2} + \boldsymbol{\Psi}^{n-1/2}}{2}, \tag{A8a}$$

$$\boldsymbol{M}\frac{\boldsymbol{\Phi}_i^{n+1} - \boldsymbol{\Phi}_i^n}{\Delta t} = -\boldsymbol{M}_{\xi i}\frac{\boldsymbol{\Phi}_i^{n+1} + \boldsymbol{\Phi}_i^n}{2} + c_0^2\boldsymbol{B}_{i,a_i}\frac{\boldsymbol{P}^{n+1} + \boldsymbol{P}^n}{2} + c_0^2\boldsymbol{B}_{i,b_i}\boldsymbol{\Psi}^{n+1/2}, \tag{A8b}$$

$$\frac{\boldsymbol{\Psi}^{n+1/2} - \boldsymbol{\Psi}^{n-1/2}}{\Delta t} = \boldsymbol{P}^n, \tag{A8c}$$

with initial conditions

$$\boldsymbol{P}^0 = 0,\ \boldsymbol{P}^1 = 0, \tag{A8d}$$

$$\boldsymbol{\Phi}_i^0 = 0,\ \boldsymbol{\Phi}_i^1 = 0,\ \forall i = 1,2,3, \tag{A8e}$$

$$\boldsymbol{\Psi}^0 = 0,\ \boldsymbol{\Psi}^1 = 0. \tag{A8f}$$

Note that (A8) corresponds to a purely explicit scheme, where all the unknowns can be calculated at time step $n+1$ from values already known from previous steps. Solving (A8) at time step $t = n+1$ involves

(1) Use (A8c) to compute $\boldsymbol{\Psi}^{n+1/2}$;
(2) Insert $\boldsymbol{\Psi}^{n+1/2}$ into (A8a) and compute $\boldsymbol{P}^{n+1}$;
(3) Update $\boldsymbol{\Phi}_i^{n+1}$ using (A8b), $\boldsymbol{\Psi}^{n+1/2}$ and $\boldsymbol{P}^{n+1}$.

To fasten all computations, matrix inversion is avoided as usual by means of a lumped approximation for all mass matrices (A7) (Hughes, 2000).

The system of equations (A8) constitutes the final numerical scheme that has been used for all the computational simulations in this work.

Abramowitz, M., and Stegun, I. (**1970**). *Handbook of Mathematical Functions* (Dover, New York), Chap. 17.

Arnela, M., and Guasch, O. (**2012**). "Adaptation of the experimental two-microphone transfer function method to compute the radiation impedance of ducts from numerical simulations," in *Proc. of ICSV19* (Vilnius, Lithuania).

Berenger, J. (**1994**). "A perfectly matched layer for the absorption of electromagnetic waves," J. Comput. Phys. **114**, 185–200.

Boonen, R., Sas, P., Desmet, W., Lauriks, W., and Vermeir, G. (**2009**). "Calibration of the two microphone transfer function method with hard wall impedance measurements at different reference sections," Mech. Syst. Signal Process. **23**, 1662–1671.

Chung, J. Y., and Blaser, D. A. (**1980**). "Transfer-function method of measuring in-duct acoustic properties. I. Theory," J. Acoust. Soc. Am. **68**, 907–913.

Codina, R. (**2008**). "Finite element approximation of the hyperbolic wave equation in mixed form," Comput. Methods Appl. Mech. Eng. **197**, 1305–1322.

Dalmont, J. P., Nederveen, C. J., and Joly, N. (**2001**). "Radiation impedance of tubes with different flanges: Numerical and experimental investigations," J. Sound Vib. **244**, 505–534.

Fletcher, N. H., and Rossing, T. D. (**1988**). *The Physics of Musical Instruments* (Springer-Verlag, New York), Chap. 8.

Fromkin, V. (**1964**). "Lip positions in American English vowels," Language Speech **7**, 215–225.

Grote, M., and Sim, I. (**2010**). "Efficient PML for the wave equation," Global Science Preprint, arXiv: math.NA/1001.0319v1.
Gutiérrez-Vega, J. C. (**2000**). "Formal analysis of the propagation of invariant optical fields in elliptic coordinates," Ph.D. dissertation, Instituto Nacional de Astrofísica, Óptica y Electrónica, Puebla, México.
Hannukainen, A., Lukkari, T., Malinen, J., and Palo, P. (**2007**). "Vowel formants from the wave equation," J. Acoust. Soc. Am. **122**, EL1–EL7.
Hughes, T. J. R. (**2000**). *The Finite Element Method. Linear Static and Dynamic Finite Element Analysis* (Dover, New York), Chap. 7.
Ihlenburg, F. (**1998**). *Finite Element Analysis of Acoustic Scattering, Applied Mathematical Sciences* (Springer, Berlin), Chap. 2.
ISO 10534-2 (**1998**). Acoustics—Determination of sound absorption coefficient and impedance in impedance tubes—Part 2: Transfer-function method (International Organisation for Standardization, Geneva, Switzerland).
Jang, S.-H., and Ih, J.-G. (**1998**). "On the multiple microphone method for measuring in-duct acoustic properties in the presence of mean flow," J. Acoust. Soc. Am. **103**, 1520–1526.
Lowson, M. V., and Baskaran, S. (**1975**). "Propagation of sound in elliptic ducts," J. Sound Vib. **38**, 185–194.
Matsuzaki, H., Miki, N., and Ogawa, Y. (**2000**). "3D finite element analysis of Japanese vowels in elliptic sound tube model," Electron. Comm. Jpn. **3**(83), 43–51.
Morfey, C. L. (**1969**). "A note on the radiation efficiency of acoustic duct modes," J. Sound Vib. **9**, 367–372.
Morse, P. M., and Ingard, K. U. (**1968**). *Theoretical Acoustics* (McGraw-Hill, New York), Chap. 7.
Motoki, K. (**2002**). "Three-dimensional acoustic field in vocal-tract," Acoust. Sci. Technol. **23**, 207–212.
Munjal, M. L. (**1987**). *Acoustics of Ducts and Mufflers* (Wiley, New York), Chaps. 1 and 6.
Oliveira, J. M. G. S., and Gil, P. J. S. (**2010**). "Propagation of sound in ducts with elliptical cross-section and lined walls," in *Proc. of Inter-noise'10* (Lisbon, Portugal).
Sivian, L. J. (**1937**). "Sound propagation in ducts lined with absorbing materials," J. Acoust. Soc. Am. **9**, 77.
Story, B. H. (**2008**). "Comparison of magnetic resonance imaging-based vocal tract area functions obtained from the same speaker in 1994 and 2002," J. Acoust. Soc. Am. **123**, 327–335.
Švancara, P., and Horáček, J. (**2006**). "Numerical modelling of effect of tonsillectomy on production of Czech vowels," Acta Acust. **92**, 681–688.
Takemoto, H., Mokhtari, P., and Kitamura, T. (**2010**). "Acoustic analysis of the vocal tract during vowel production by finite-difference time-domain method," J. Acoust. Soc. Am. **128**, 3724–3738.
Vampola, T., Horáček, J., and Švec, J. G. (**2008**). "FE modeling of human vocal tract acoustics. Part I: Production of Czech vowels," Acta Acust. **94**, 433–447.
Vampola, T., Laukkanen, A. M., Horáček, J., and Švec, J. G. (**2011**). "Vocal tract changes caused by phonation into a tube: A case study using computer tomography and finite-element modeling," J. Acoust. Soc. Am. **129**, 310–315.
Zhou, X., Espy-Wilson, C. Y., Boyce, S., Tiede, M., Holland, C., and Choe, A. (**2008**). "A magnetic resonance imaging-based articulatory and acoustic study of 'retroflex' and 'bunched' American English /r/," J. Acoust. Soc. Am. **123**, 4466–4481.
Zorumski, W. E. (**1973**). "Generalized radiation impedances and reflection coefficients of circular and annular ducts," J. Acoust. Soc. Am. **54**, 1667–1673.